Environ Monit Assess (2022) 194: 547
https://doi.org/10.1007/s10661-022-10213-6

Analysis of algal bloom intensification in mid-Ganga river, India, using satellite data and neural network techniques

Rajarshi Bhattacharjee · Arpit Gupta · Nilendu Das · Ashwani Kumar Agnihotri · Anurag Ohri · Shishir Gaur

Received: 3 January 2022 / Accepted: 20 June 2022 / Published online: 1 July 2022

Abstract River Ganga is one of the most significant rivers in the country. This river is the adobe for numerous aquatic species and microorganisms. The color of the river suddenly changed to green due to the rise of algal bloom in the Varanasi and nearby regions of the river Ganga during May–June 2021. These algal blooms can be detrimental to the aquatic animals of the river. This study analyzes the occurrence and the possible reasons for the algal bloom generation in the river for the considered stretch. Several factors like nutrient accumulation in the river through agricultural run-off, warm river temperature, low flow condition of the river, thermal stratification, and less turbid river water can be considered as possible reasons for algal bloom development. In this work, the optical remote sensing-based Sentinel 2 datasets have been used for the duration of mid-May 2021 to mid-June 2021. These datasets have been processed in the Google Earth Engine (GEE) platform, and chlorophyll concentration has been calculated using different satellite-based indices or band ratios. The chlorophyll concentration measurements have quantified the algal bloom growth. These indices or band ratios have been analyzed using several artificial neural network (ANN) architectures like multilayer perceptron (MLP) and radial basis function (RBF) along with the in situ values. It has been found that chlorophyll concentration has been highest for the mid-June 2021 time period in the considered river stretch.

Keywords Optical remote sensing · Band ratios · MLP · RBF · GEE · Thermal stratification

R. Bhattacharjee · N. Das (✉) · A. K. Agnihotri · A. Ohri · S. Gaur
Department of Civil Engineering, Indian Institute of Technology (BHU), Varanasi 221005, India
e-mail: dasnilendu2016@gmail.com

R. Bhattacharjee
e-mail: rajbhatt78645@gmail.com

A. K. Agnihotri
e-mail: ashwanika.rs.civ15@itbhu.ac.in

A. Ohri
e-mail: aohri.civ@iitbhu.ac.in

S. Gaur
e-mail: shishirg.civ@iitbhu.ac.in

A. Gupta
Department of Electronics and Communication Engineering, National Institute of Technology Raipur, Raipur, 492010, India
e-mail: arpit30nitrr@gmail.com

Introduction

The Ganga river, situated in the northern part of India (internationally known as the Ganges), is one of the major rivers across the globe. Approximately 40% of the Indian population (~540 million people) lives within its basin (Bowes et al., 2020). The Ganga river is the abode for various species, and it can bestow humanity with several ecosystem services

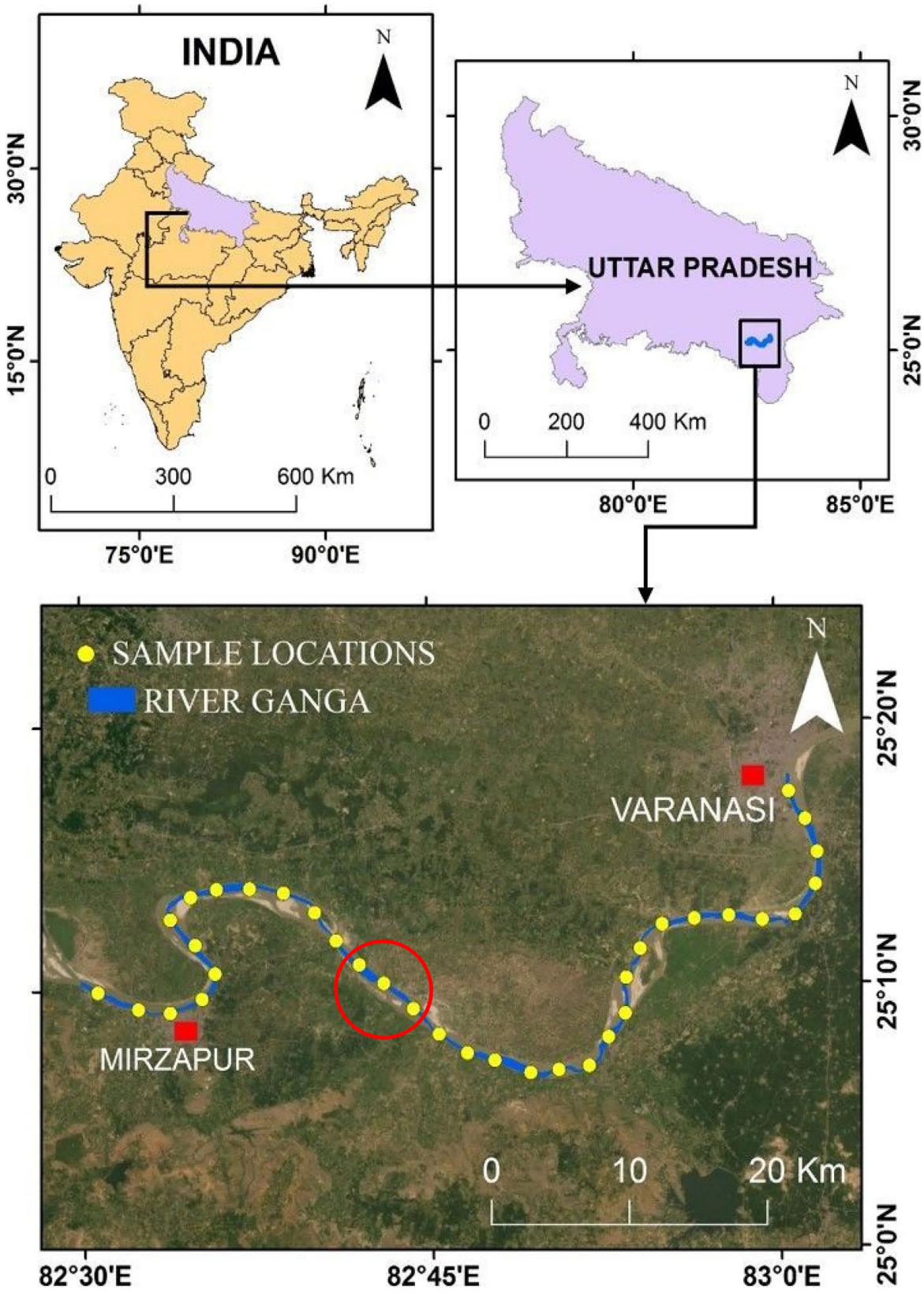
INDIA
N
30°0'N
15°0'N
0
300
600 Km
75°0'E
90°0'E
UTTAR PRADESH
N
30°0'N
25°0'N
0
200
400 Km
80°0'E
85°0'E
SAMPLE LOCATIONS
RIVER GANGA
N
VARANASI
MIRZAPUR
0
10
20 Km
25°20'N
25°10'N
25°0'N
82°30'E
82°45'E
83°0'E

◂ **Fig. 1** Geolocation map of the study area. The samples rounded by the red circle have been collected between 10:15 AM and 10:45 AM for all three sampling dates

(Jaiswal & Pandey, 2019). The river Ganga is the primary source of water for the agricultural fields and industrial units located in the vicinity of the river. It can produce an income source for the people associated with it (Haritash et al., 2016; Trivedi, 2010). Human intervention and industrial and agricultural waste can cause a bacterial and algal bloom in the river. Phosphate, sulfur, and nitrate are the nutrients that help the algae grow. The algae release the neurotoxin microcystin that will pose a threat to aquatic lives. The same scenario can be observed in river Ganga (Dixit et al., 2017; Tare et al., 2003; Zanchett & Oliveira-Filho, 2013). The measurement of the chlorophyll in water can be used as the yardstick to determine the algae in the water (Devi et al., 2008; Lee et al., 2005).

Nowadays, remote sensing technology and satellite-based imageries have been used abundantly to measure the chlorophyll in the water bodies. The physical properties of distant objects can be computed using emitted or reflected energy, which is the primary explanation for this technology. Compared to traditional methods, remote sensing datasets can provide the synoptic view, repetitive coverage of a particular place to observe the change and information of an area beyond visible wavelengths, which is otherwise impossible to detect through the naked eyes (Budd et al., 2001; Roy et al., 2017). In the year 2010, Google had created a modern technology for processing the satellite imageries, known as GEE (Google Earth Engine). Massive satellite datasets can be processed using GEE technology. GEE is a cloud-based computing model, and this model is freely available on the web platform (Gorelick et al., 2017; Zurqani et al., 2018).

For the last 1.5 years, the whole world has been suffering from the pandemic known as COVID-19, caused due to the novel coronavirus strain. It has been one of the most virulent diseases that affect human lives in more than 200 countries, including India (Chauhan & Singh, 2020; Patel et al., 2020). In this coronavirus scenario, some of the media reported about the river Ganga getting green in the Varanasi region during May 2021 (Jaiswal, 2021). The media report states that scientists have analyzed that the greenish appearance of the river could be due to microcystis algae. Some other scientists are also claiming that the rainfall can also be an additional factor for the increase in the nutrients in the river Ganga, which can make the river green due to the algal bloom spread. But in general, the change in the color of river water is a major cause of concern for the local people who take a daily bath in the river. During the same period in May 2020, the river water was clean due to less pollution discharge in the river because of the lockdown implemented by the Indian government (Garg et al., 2020).

Field sampling for the river chlorophyll (Chl-a) measurement has been done. The satellite imageries have been utilized in this study to detect the presence of the green algae in the river Ganga for the Varanasi and its nearby areas by analyzing the chlorophyll spread. Statistical modeling and artificial neural network (ANN) techniques have been applied to determine the algal spread in the river for the considered stretch from mid-May 2021 to mid-June 2021.

Materials and methods

Study area

The study stretch that has been chosen for this analysis is situated between Varanasi and Mirzapur. This stretch is located in southeastern Uttar Pradesh, a state of India, between the coordinates 82.49°E, 25.17°N to 83.00°E, 25.29°N. In terms of the geomorphological unit, this segment of the river comes under the central Ganga plains. The river plain in this region is flat alluvial in nature, having a slight eastward gradient and shallow depression. In this segment, the average width of the river varies between 700 and 750 ms. The average height of this region is 76.19 m above the mean sea level (Pandey & Singh, 2017; Rai et al., 2010). The summer season in this region is more dominant in this region than the winter season because the summer season has a longer duration. The temperature in this region for the winter season lies between 5 and 15 °C, primarily, and for the summer season, the temperature range varies between 32 and 47 °C. The average annual precipitation in this region is 1110 mm (Das et al., 2020). In Fig. 1, the map of the study area has been drawn.

In situ Chl-ameasurement

The field sampling was done on 15 May, 30 May, and 14 June 2021 to measure the Chl-a concentration in the river. The concentration has been measured using YSI ProDSS Water Quality Meter. The Chl-a concentration values have been measured mainly at the center of the river channel at 0.5 m below the water surface. Simultaneously, GPS coordinates were also recorded for those points with a handheld portable GPS system (Garmin Ltd. etrex-12 channel global positioning system). Thirty-five samples have been measured throughout the study stretch for each of those sampling dates.

Satellite data description

Sentinel-2 (S-2) images have been used in this study, and under the Copernicus S-2 mission, the satellites have been launched. This mission consists of two satellites, namely Sentinel-2A (S2A) and Sentinel-2B (S2B). These are multi-spectral (MSI) satellites. S2A and S2B were commissioned in orbit in 2015 and 2017. Analysis of the lake ecology and retrieving information about the water quality at finer scales are some of the significant usages of the S2 imageries (Bresciani et al., 2018; Bhattacharjee et al., 2021). Level 2 products of S2 images have been available on the GEE platform (Li et al., 2019; Bhattacharjee et al., 2021). The spatial resolution of blue, green, red, and NIR (Near Infrared) bands is 10 m as compared to 30-mresolution for the same bands in the LANDSAT satellite. S-2 imager has a revisit time of 10 days, but when both the imagers are operational, the revisit time decreases to 5 days. The temporal resolution of Sentinel satellites is better than LANDSAT satellites because the LANDSAT satellites have a 16-day temporal resolution (Van der Werff & Van der Meer, 2016; Gorji et al., 2020). The GEE platform has been used for processing the S-2 images. Sen2cor atmospheric correction technique has already been applied to the GEE platform. The datasets of S2A and S2B, which completely covered the entire study stretch, have been collected for the month of May and June 2021. The S-2 satellite images dated 15 May, 30 May, and 14 June 2021 have been chosen for this study.

Indices calculation in the GEE platform and selecting indices using regression model(s) based on statistical parameters

The biogeochemical characteristics of the water body have been the driving force for selecting the proper indices. Researchers encounter a significant challenge in selecting the indices to measure Chl-a in inland waters. The challenge is that the presence of inorganic suspended solids (ISS) and color dissolved organic matter (CDOM) have higher values, and their concentrations in the water are not always correlated with Chl-a (Palmer et al., 2015). Most of the researchers incorporate the NIR-to-red ratio and the green-to-red ratio-based indices to measure Chl-a in the inland water. These ratio-based indices will remove the absorption overlap effect of CDOM and ISS. The absorption effect of CDOM and ISS have been prominent in the blue region of the electromagnetic (EM) spectrum (Ha et al., 2017a, b). In addition to that, water reflectance has been measured by different satellites at various wavelengths. So a single algorithm lacks versatility for precise calculation of Chl-a. For example, the positioning of spectral bands in LANDSAT-8 is such that NIR-to-red ratio estimation for Chl-a will not give explicit results. S-2 satellite has red-edge bands, and the red-edge1 to red ratio will give a convincing result in determining the Chl-a concentration. So for different satellites, distinct band ratios need to be applied for Chl-a estimation (Gholizadeh et al., 2016; Ha et al., 2017a, b).

The S-2 satellite has red-edge bands, and the analysis from those satellite images shows that chlorophyll has a peak in the red-edge wavelength range along with the green wavelength range (Huete, 2004; Chen et al., 2017; Bramich et al., 2021). For this study, the reflectance values from S-2 images over a 3×3 pixels grid encompassing the sampling point to reduce noise have been used (Han & Jordan, 2005). In this study, six bands of the S-2 images have been used for indices generation. The central wavelength and spatial resolution of the bands used in this analysis have been tabulated in Table 1.

For the calculation of these indices, the S-2 images dated 15 May, 30 May, and 14 June 2021 have been processed in the GEE platform. Three images have been selected for this analysis because the other images in this period have very high cloud cover. Within a

Table 1 Characteristics of the S2A bands used

Sentinel-2 bands	Central wavelength (nm)	Spatial resolution (m)
Band 2-blue	490	10
Band 3-green	560	10
Band 4-red	665	10
Band 5-red edge 1	705	20
Band 7-red edge 3	783	20
Band 8-NIR	842	10
Band 8A-NIR narrow	865	20

short time frame, the GEE platform processes all the images. By using the Google earth pro software, the shapefile of the study area has been drawn, and then in the GEE domain, that shapefile has been imported for the indices calculation. Statistical modeling has been applied in this study to select the few better band combinations for Chl-a estimation from S-2 images.

Three statistics-based regression models, namely linear, exponential, and power models, have been chosen. The most suited band ratios and the correlated bands with in situ data have been integrated and tested by four trendline functions: linear, exponential, logarithmic, and power. The best regression model has been chosen on the basis of the root mean square percent error (RMSPE). The best model has the least RMSPE. The formula for the RMSPE has been given as

$$\mathrm{RMSPE} = \sqrt{\frac{1}{n}\sum_{i=1}^{n}\left(\frac{X_{\mathrm{est}} - X_{\mathrm{act}}}{X_{\mathrm{act}}}\right)^{2}} \times 100 \quad (1)$$

Where n represents the number of samples, X_{est} represents the value generated from the model, and X_{act} is the actual value obtained from the field sampling.

Then for the best model, all the generated indices were simulated using statistical parameters like r (Pearson's correlation coefficient), $R.^2$ (coefficient of determination), RMSPE, and mean absolute percentage error (MAPE). The formula for the MAPE has been given as

$$\mathrm{MAPE} = \frac{1}{n}\sum_{i=1}^{n}\frac{|X_{\mathrm{est}} - X_{\mathrm{act}}|}{X_{\mathrm{act}}} \times 100 \quad (2)$$

The uncertainty factor has been associated with the statistical model. This factor has been minimized in this study by randomizing the model 25 times for each of the input band ratios.

Finally, some of the indices have been selected, which have better r and R^2, and lower RMSPE and MAPE. The rest of the others have been rejected. Then these selected indices further have been given as input to the neural network models for Chl-a estimation.

Chl-a estimation using artificial neural networks

Multilayer perceptron network

The artificial neural networks (ANN) provides a modified approach for assessing complex relationships among the variables without considering assumptions. In the case of remote sensing-based analysis, the input and other supporting variables establish an equation with biophysical factors. These biophysical factors have been depicted as output variables (Mas & Flores, 2008). Many non-linear relationships can be modeled by using ANN without having a priori knowledge of the type of nonlinearity. This kind of modeling cannot be performed using non-linear regression models (Palani et al., 2008). In this study, multilayer perceptron (MLP) neural network has been used, and MLP works well to capture the non-linear relationship. The MLP ANN model has been composed of input, hidden, and output layers. The datasets have been inserted into the model through input layers. The next stage of the model comprises hidden layers, which have been used for information processing. Then this processed information goes to the output layers. The neurons have been known as the basic building blocks for these layers. The neurons have been defined using the algebraic functions, which depict nonlinearity. The parameters for these functions have been decided by the boundary values (Singh et al., 2009). The passing signals have been repeatedly modified by neurons using the wright and transfer function until they reach the output layer. The number of neurons in a network depends upon the network architecture. The input and hidden layers have been connected through weights, and these weights have been usually evaluated by system training. The weighted inputs have been added to the hidden layers, and then these layers generate the output using the transfer function. The significant variations among the different ANN models have been the

network architecture, weight determining techniques, and activation function used (Palani et al., 2008). One of the widely used learning algorithms applied in ANN has been the backpropagation (BP) technique. The training algorithm arrives at the best fit condition through the error redistribution technique. Several stages have been involved in the development of the BP technique. The first step is determining the important input parameters by incorporating the statistical methods. The field datasets have been grouped into training (74 samples) and validation (31 samples) to check the model's efficacy. In the next step, randomly selected training and test datasets have been inserted into the network. In general, 30% of the total datasets represent the test datasets. The weighted inputs have been aggregated using the hidden layers, and these hidden layers also generate the output value using the transfer function. Levenberg–Marquardt algorithm (LMA) has been applied to compute the weights. In comparison to the conventional gradient descent algorithm, the LMA computes the weight more rapidly (Prasad et al., 2020). This analysis has incorporated the *tansig* function as the transfer function from the input layer to the hidden layer. From the hidden layer to the output layer, *purelin* has been selected as the transfer function (Guo et al., 2016).

Radial basis function network

The radial basis function (RBF) networks are special feed-forward networks that have a single hidden layer. These kinds of networks contain the linear and non-linear types of neurons. The non-linear functions like Gaussian and sigmoid have been used for the hidden layer neurons. In addition to that, a linear function has been placed in output layer neurons as its transfer (activation) function. For the function approximation problem, the linear output layer transfer function has been used (Kopal et al., 2019; Nguyen & Keip, 2018). There is no inter-connection between the neurons on the same layer. All the neurons of the next layer have been connected to a single neuron of the previous layer. In the input layer, the information has been inserted. The input signal does not get affected by the transfer function. In this architecture, the input data has been transferred from the user. The hidden layer of the network assists the input data in propagating through them in a forward direction so that they can reach the output layer. This network follows the feed-forward network structure rule (Kopal et al., 2019). The information transferring process happens from the linear input layer to the non-linear hidden layer. The information transfer has been executed in such a way that each hidden neuron's output becomes reversely proportional to the Euclidean distance. This distance has been measured between the center of the RBF of a particular neuron and the input vector. (Xu & Gupta, 2019). For the Gaussian activation function, the center of the symmetrical Gaussian bell curve has been represented by the weights of hidden layer neurons. The weights have been predecided in such a way that the Gaussian activation function encloses the entire input space. Each Gaussian function traverses only to a narrow domain of the input space where the Gaussian has been centered (Ressom et al., 2007; Davydov & Oanh, 2011). The output layer has estimated the aggregation of biases and weights of total RBFs output. The application and development of the RBF-ANN architecture have been the estimation of the optimal number of hidden neurons as well as the weightage determination of the output layer. For successful learning, an important step has been implemented by bias value, which shifts the activation function either right or left side. The shift occurred due to the biasing assist in generating a better fitting curve for the data as well as the better prediction model creation for ANN output (Pislaru & Shebani, 2014). In the learning algorithm, the width and position of RBF centers and the linear weights associated with each output neuron have been modified at each iteration. The RBF-ANN is also an error-back-propagation ANN. This architecture requires less time for learning as compared to MLP architecture because all of the inputs of RBF-ANN have been assigned directly into the hidden layer by not giving any weightage. The error signal has been incorporated to adjust the weight between the hidden and the output layer. When the center of each RBF comes very near to the input vector, then the network learning process gets completed. The error generated by the output network has been under the desirable limit in such a scenario. So, the functional dependence approximation within the variables can be represented by a combination. This combination has been linear in nature for an optimal number of RBFs with acceptable widths which have been suitably positioned (Davydov & Oanh, 2011; Kopal et al., 2019). A Gaussian function has been implemented as the RBF of the hidden layer neurons in the form of (Davydov & Oanh, 2011)

$$\varphi_j(x_i) = \exp(-\frac{||x_i - \mu_j||^2}{2\sigma_j^2}) \quad (3)$$

where $\varphi_j(x_i)$ represents the response of the jth hidden neuron corresponding to its input $x_{i,}$ and the terms σ_j and μ_j denote the centroid and spread width, respectively.

$$d_j(x_i) = ||x_i - \mu_j||^2 \quad (4)$$

The term $d_j(x_i)$ represents the Euclidean distance between the elements of the input vector x_i and the corresponding centroid of Gaussian $\mu_{j.}$ The datasets have also been divided into a 70:30 ratio for training and testing for this model.

In this study, the neural network models have been developed with three layers (input, hidden, and output) in the Google COLAB environment (a python-based open-source platform). The input layer consists of six selected input variables. A total of 70% of the datasets have been used for model training, and 30% for model testing. The number of nodes depends on the complexity of the approximated function and sample size. The output layer was of the Chl-a concentration of the sampling points, and the output layer had a single node. The initial learning rate for both ANN models has been set as 0.01, and the Adam optimization function has been used for both models. The structure of the ANN model(s) is shown in Fig. 2.

The overall flowchart of the methodology adopted for this study has been drawn in Fig. 3.

Results and discussion

Chl-a concentration variation in the study stretch for in situ measurement

The concentration of the Chl-a variation for in situ measurement has been shown through a violin plot in Fig. 4.

Boucher et al. (2018) stated that algorithm efficiency and performance could be reduced if the time interval between satellite acquisition day and in situ measurement day increases. In this study, the in situ measurement was done on the same date as the satellite overpass over the study stretch. The average air temperature for the region has been recorded as 31.75 °C on 15 May, 29.77 °C on 30 May, and 32.54 °C on 14 June. Chl-a concentration varies between 7 and 19 µg/L on 15 May 2021 with a standard deviation (SD) of 3.65 µg/L. On 30 May 2021, the concentration of the Chl-a ranges between 36 and 68 µg/L with an SD of 8.72 µg/L. The Chl-a concentration was highest on 14 June 2021 and; it lies between 56 and 91 µg/L having an SD of 9.39 µg/L. One of the probable reasons for the surge in the Chl-a concentration in the river is the increase in rainfall amount in mid-June as compared to mid-May. The rainfall increases the river depth marginally as, in this case, the average depth of the river throughout the study stretch on 15th of May has been calculated as 7.86 m, while the average depth increased to 8.03 m on 30th of May. In this study, the river depth has been considered as a proxy variable for the thermal stratification. It has been assumed that if the river depth has increased, the river thermal stratification also gets enhanced. The lower layer of the thermally stratified water body gets exhausted with oxygen, leading to nutrient release from the sediments. The nutrients from the colder water layer may enhance the algal growth in the uppermost layer of the water body (Weinke & Biddanda, 2019). The chlorophyll-a variation, along with the river depth, has been shown in Fig. 5a.

The river flow velocity has also been recorded for the three sampling dates. From the velocity graph, it can be seen that on all the three considered dates, the velocity of the river has been less than 1 m/s.

The "*t*-test: paired two sample for means" analysis has also been performed between the depth and chlorophyll-a for the two dates, i.e., 15 and 30 May 2021, at a confidence level of 95% ($\alpha = 0.05$). The analysis outcome has been tabulated in Tables 2 and 3. In these tables, variable 1 corresponds to river depth, and variable 2 corresponds to chlorophyll concentration.

From the above two tables, it can be seen that in *t*-tests, the critical *t*-value is less than the modulus of the calculated *t*-value (t stat value). The *P*-value (randomness) has been less than the critical *t* value. So the alternate hypothesis that tells the river depth affects the chlorophyll concentration has been accepted. The null hypothesis, which ascertains the river depth has no effect on chlorophyll concentration, has been rejected.

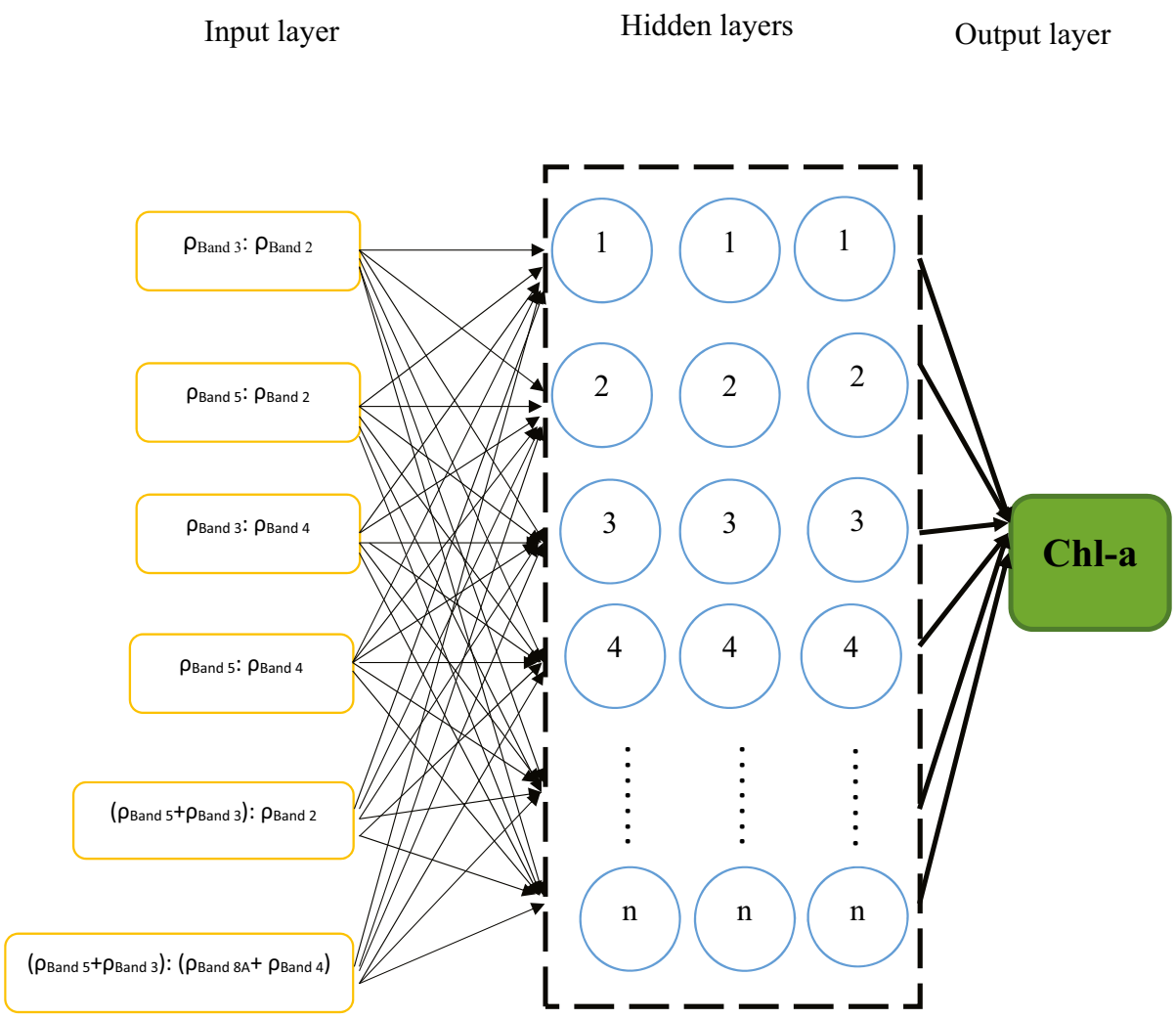

Fig. 2 ANN architecture implemented for this analysis

According to the media reports, environmental and river scientists are showcasing the increase in the rainfall of this region as the primary reason for the algal bloom. The scientists claim that more fertilizers are getting mixed with the river water due to the improved precipitation. The fertilizers mostly contain phosphate, sulfur, and nitrate, which in turn can act as nutrients that can be helpful for algal growth. The rainfall graph of the region for the time period between 1 May 2021 and 22 June 2021 is given in Fig. 6. The rainfall dataset has been downloaded from the India Water Resources Information System (India-WRIS) portal.

Analysis of the spectral curve and best regression model for the assessment of the band ratios

For each day of the in situ sampling, ten sampling points out of 35 points have been chosen for the spectra generation. The spectral curve for 14 June 2021 has been provided in Fig. 7.

Four of the most suited band ratios, namely $\rho_{\text{Band 5}}$:$\rho_{\text{Band 2}}$, $(\rho_{\text{Band 5}}+\rho_{\text{Band 3}})$:$\rho_{\text{Band 2}}$, $\rho_{\text{Band 5}}$:$\rho_{\text{Band 4}}$, and $\rho_{\text{Band 3}}$:$\rho_{\text{Band 2}}$, have been chosen to decide the best regression model. The RMSPE of the power model has the lowest value, so this regression model has been selected further to distinguish between all the suited and non-suited band ratios. The average

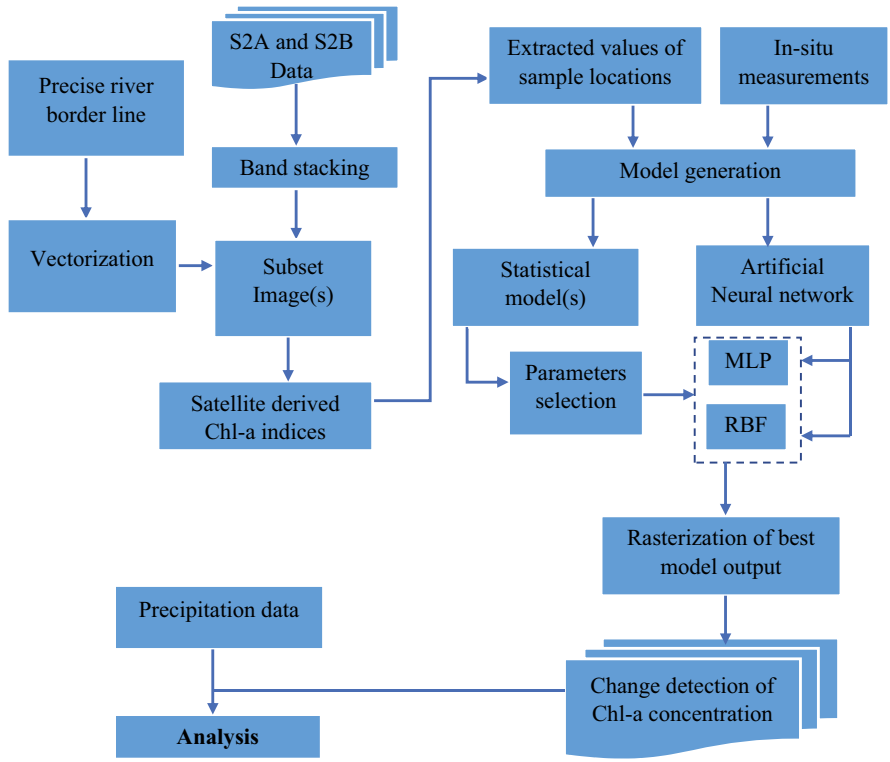

Fig. 3 Flowchart of the methodology

RMSPE of the four models for the four most suited band ratios has been tabulated in Table 4.

In this study, ten band ratios have been analyzed using the power model, and out of those ten band ratios, six ratios have been selected, and the remaining four have been rejected for further process. The performance of the band ratios for the power model is given in Table 5.

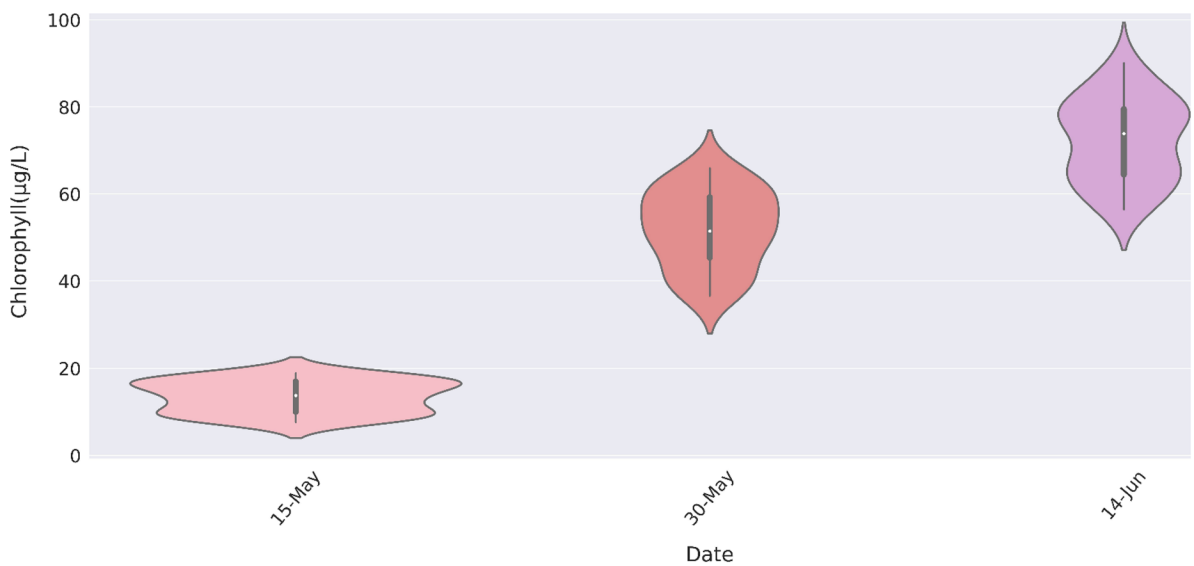

Fig. 4 Variation of the Chl-a concentration for all the sampling dates

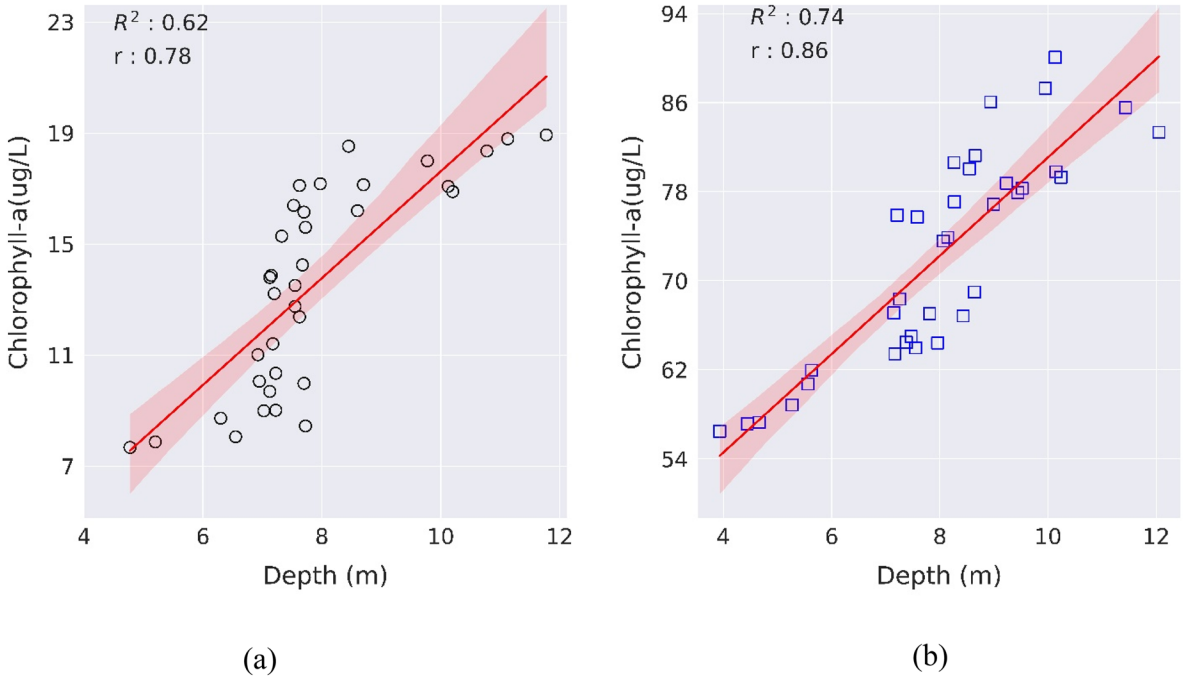
R^2 : 0.62
r : 0.78
Chlorophyll-a(ug/L)
Depth (m)
(a)
R^2 : 0.74
r : 0.86
Chlorophyll-a(ug/L)
Depth (m)
(b)

(a)

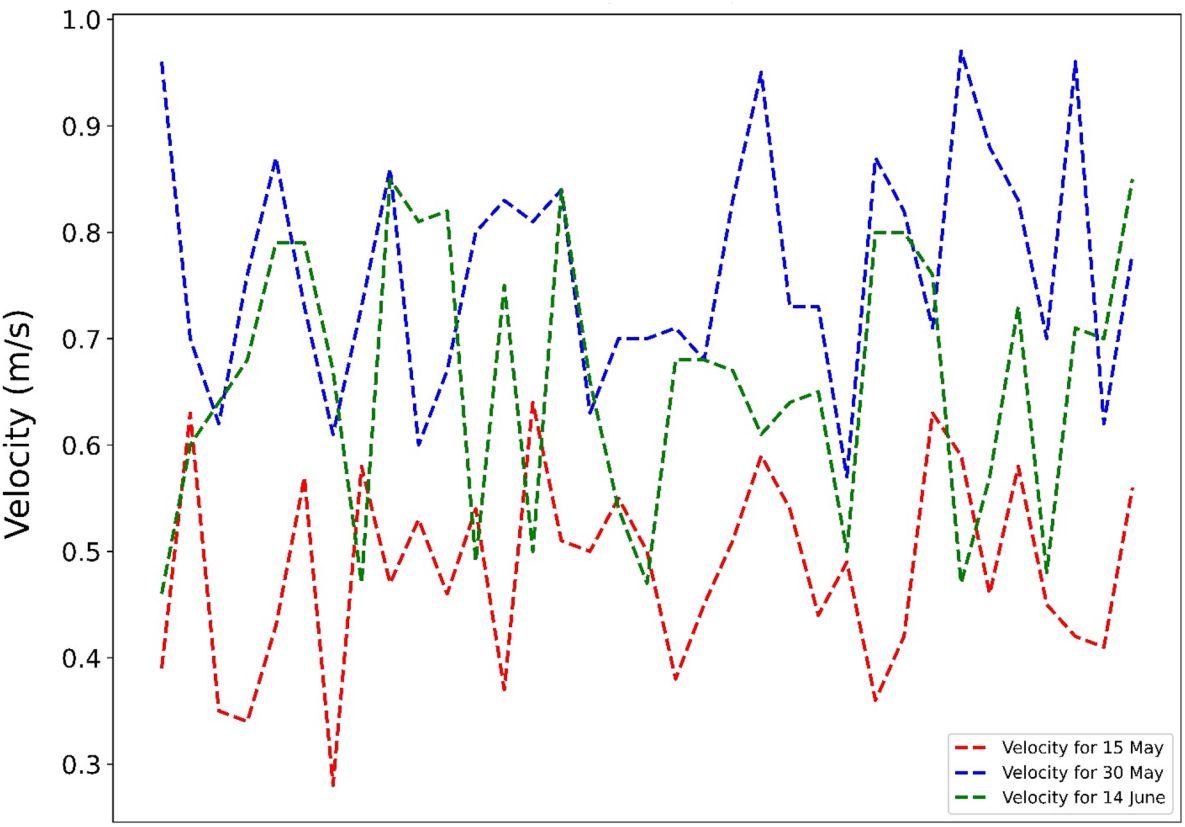
Velocity (m/s)
Velocity for 15 May
Velocity for 30 May
Velocity for 14 June

(b)

◂**Fig. 5** **a** Regression plot showing the variation between chlorophyll-a and river depth for **a** 15 May 2021 and **b** 30 May 2021**. b** Line graph showing the river flow velocity for the three considered dates. The measurement has been done from the Mirzapur side to the Varanasi side

For all of the 105 sample points, the analysis has been done. If a band ratio satisfies the four statistical parameter criteria, then only it has been selected. The band ratio $\rho_{\text{Band 8}}$:$\rho_{\text{Band 4}}$ fulfills two statistical criteria out of the four, so it has still been rejected. The criteria and selection scenario have been depicted through a Venn diagram given in Fig. 8.

Analysis of the ANN models

ANN models procure better results as compared to statistical regression models (Duan et al., 2007; Ha et al., 2017a, b). Analysis of the Guo et al. (2016) on the Haihe River, China, illustrates that neural networks have better efficiency than regression models. In this study, two ANN models have been incorporated for Chl-a estimation. The optimal number of the nodes in the hidden layer for MLP has been 17 for this present, with a MAPE value of 3.73%. RBF has 15 nodes that produce the optimal result for this analysis with a MAPE value of 2.42%. Figure 9 shows the optimal number of nodes for both the neural network architecture. Even if the number of nodes increases, the MAPE error for both models shows an upsurge.

The regression curve for the two ANN models has been made from the test datasets of the two models. These two models randomly select the test data from the datasets. In Fig. 10, the regression plot has been drawn for the two models. It shows the relationship between the independent variable known as "Target" and the dependent variable known as "Output." The independent variable represents the in situ Chl-a concentration values, and the dependent variable portrays the predicted Chl-a concentration values by the ANN models. The RBF model has a slightly better r and R^2 value as well as marginally lower RMSPE and MAPE. The RBF model performs moderately better in this study because the low-dimensional datasets have been used for which deep-feature extraction is not mandatory. Moreover, for this study, the output results have been directly correlated with the component of input vectors (Bansal, 2017).

The scatter plot of Chl-a concentration simulated from these two ANN models for the test datasets and in situ Chl-a concentration for those exact locations has been shown in Fig. 11. The values predicted from RBF have been slightly better in accuracy as compared to the MLP model.

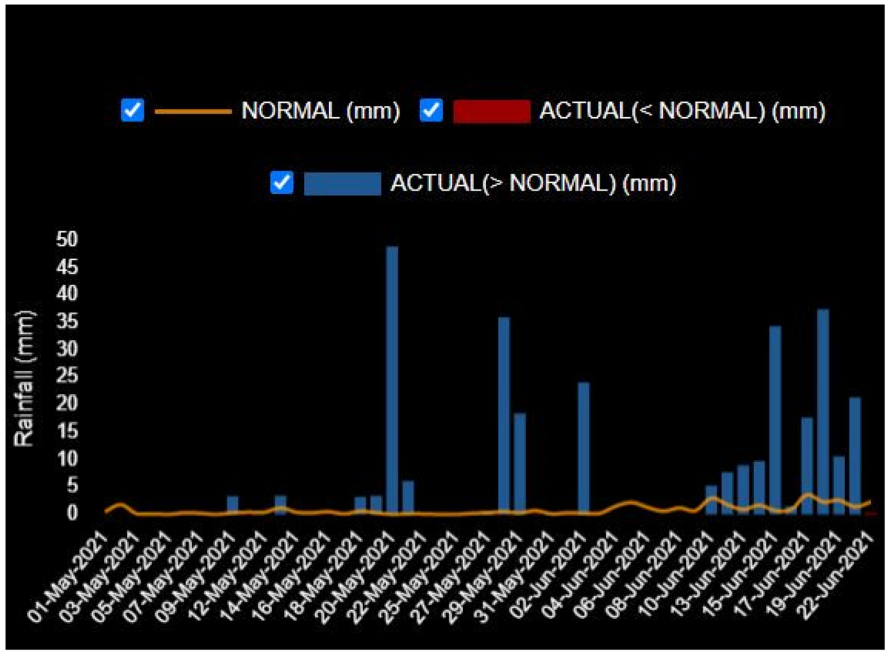

Fig. 6 Rainfall graph for the Varanasi and nearby region for the time period May 1–June 22, 2021

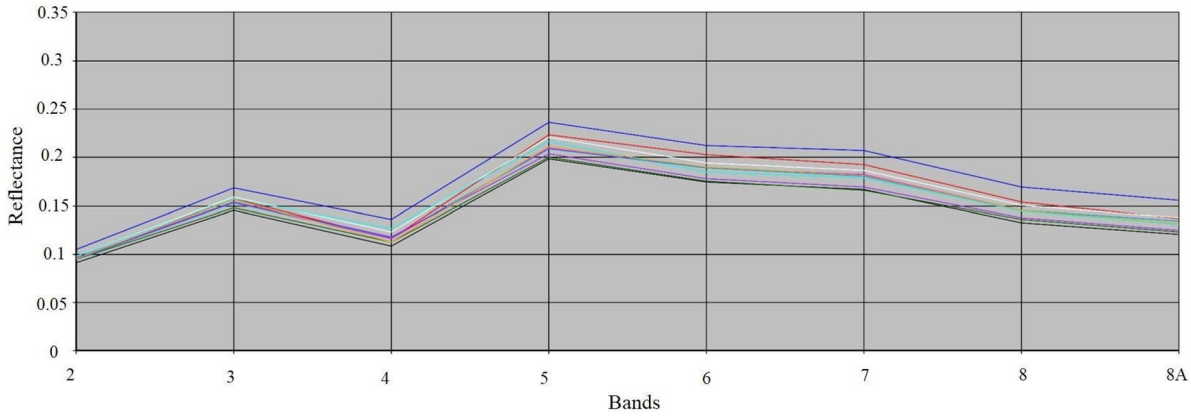

Fig. 7 Spectral reflectance curve based on S-2 bands over the study stretch. The spectral curves correspond to 10 sampling points collected on 14 June 2021

Several researchers incorporate single-day image reflectance data and single-day in situ measurement data for the model simulation (Markogianni et al., 2013; Rundquist et al., 1996). This study incorporated the multi-date in situ measurement and image reflectance values, increasing the model efficiency.

Mapping the spatial distribution of the Chl-a concentration

RBF algorithm captures the fluctuation in the Chl-a concentration level in a better manner as compared to MLP. The modified Shepard (MS) interpolation technique has been applied to interpolate the RBF model output. Franke and Nielson developed the MS technique in 1980. The inverse distance weighted least-squares method has been incorporated into this technique. The interpolators are similar to those applied in inverse distance weighting (IDW) technique. The use of local least squares eliminates the " bull's-eye" pattern (Bronowicka-Mielniczuk et al., 2019). The concentration of Chl-a varies between 6.65 and 18.08 µg/L on 15 May, but on 30 May, the concentration ranges between 34.23 and 69.47 µg/L. In June 2021, the concretion of Chl-a increased more rapidly as the algal bloom spread more swiftly, and on June 14, Chl-a concentration hovers between 58.65 and 91.87 µg/L. The spatial spread of the Chl-a concentration is shown in Fig. 12.

Table 2 *t*-Test analysis for 15th of May.

Parameters	*Variable 1*	*Variable 2*
Mean	7.862143	13.50571
Variance	2.283322	13.72756
Observations	35	35
Pearson correlation	0.784922	
df (degree of freedom)	34	
t Stat	− 12.424	
$P(T<=t)$	1.71E − 14	
t Critical	1.690924	

Assessment of the probable causes for the Chl-a concentration and algal bloom variation in the river

The media reports stated that Ganga is turning greenish in the Varanasi and nearby regions in late May 2021 (Singh, 2021). The precipitation cannot be the only sole reason for the Ganga turning green. It has been reported by the regional officer of the Central Pollution Control Board (CPCB) that on 21 May 2021, for the first time, river water turned green, and after 3–4 days, it became normal, but again, after a few days, the water turned green. If we observe the rainfall data from May 1 to May 21, 2021, then it can be noticed that before 21 May 2021, only on 20 May, the aggregate rainfall above 40 mm was recorded. Even on 16 June 2000, the aggregate precipitation above 50 mm occurred,

Table 3 *t*-Test analysis for 30th of May

Parameters	*Variable 1*	*Variable 2*
Mean	8.031714	72.38057
Variance	3.483556	90.75695
Observations	35	35
Pearson correlation	0.863259	
df (degree of freedom)	34	
t Stat	−47.7847	
$P(T<=t)$	4.63E−33	
t Critical	1.690924	

but Ganga did not turn green during that time. For May–June 2000, the precipitation graph is shown in Fig. 13.

The normal value in the rainfall graph has been calculated by considering 96–104% of the long period average (LPA). The LPA has been calculated by Indian Meteorological Department (IMD) for a period of 50 years, starting from 1951 to 2000 (Pai et al., 2017).

The temperature of the river in this region during the month of May and June mainly varies in the range between 27 and 30 °C (Saxena & Singh, 2020). The temperature range between 22 and 35 °C has been very favorable for the growth of algae (Singh & Singh, 2015). So, the temperature can also be considered one of the factors for algal growth (Wang et al., 2016).

The stable water condition of the river is also one of the many factors positively influencing algal growth. Most of the algae prefer stable water conditions with a low flow rate (Zhu et al., 2013). Global warming can be one of the factors for the low flow rate in the river because, with the increase in the river temperature, the discharge of the river gets reduced

Table 4 RMSPE values showing the efficiency of the regression models for four of the most suited band ratios

Model	RMSPE[a]
Linear	32.41
Exponential	28.23
Logarithmic	27.57
Power	17.11

[a]The values have been denoted in percentage (%).

Table 5 Performance of the band ratios for the power model using in situ Chl-a measurements and reflectance datasets ($N=105$)

S-2 band ratio	r	R^2	RMSPE[a]	MAPE[a]
B3/B2	0.7	0.57	32.2	22.8
B5/B2	0.75	0.64	30.8	21.9
B3/B4	0.67	0.55	32.9	23.1
B5/B4	0.73	0.6	31.2	22.6
(B5+B3)/B2	0.81	0.69	27.9	20.8
(B5+B3)/(B8A+B4)	0.63	0.52	33.4	23.3
B8/B4 (R)[#]	0.66	0.53	47.3	31.9
B8A/B2 (R)	0.34	0.26	66.5	39.7
B7/B4 (R)	0.44	0.34	53.3	36.4
B7/B2 (R)	0.49	0.41	49.6	33.8

[a]The values have been denoted in percentage (%)

[#]Rejected ratios have been marked with (*R*) beside them

(Van Vliet et al., 2011). Along with global warming, the water extraction for irrigation and construction of weirs and dams over the river also subside the river flow rate. According to some media reports, the Ganga basin already has 942 dams and weirs in its various tributaries. Still, many more such structures

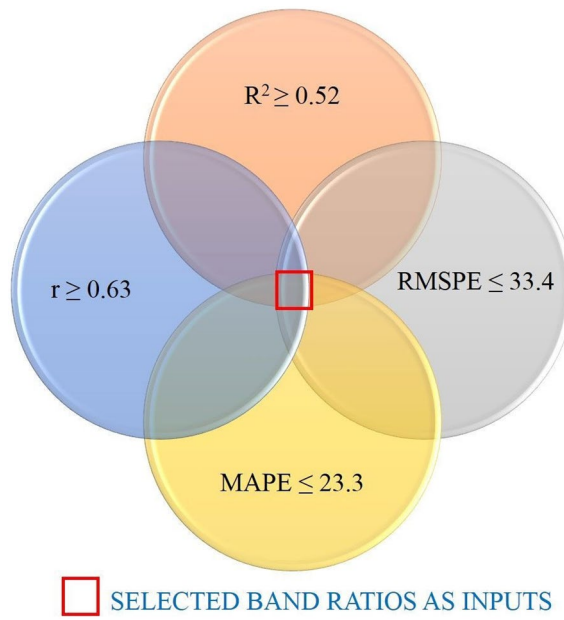

Fig. 8 Selection criteria of the band ratios as inputs to the ANN architecture(s) using logical operator

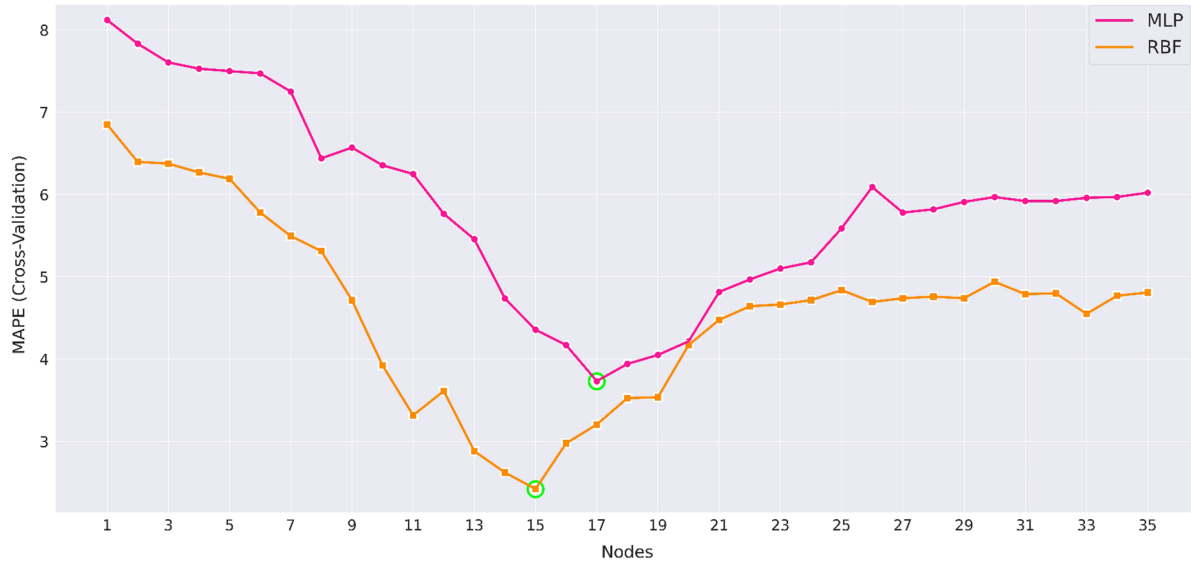

Fig. 9 Performance evaluation of MLP and RBF architectures based on the number of nodes present in the hidden layer (MAPE values are in %)

will be built in the near future (Misra, 2019). The region of Varanasi and the nearby stretch has been mainly covered by agricultural land (Mishra et al., 2018). The population of this region is increasing, and so is the demand for food as well. Rice is one of the major crops of this region, and the irrigation area for rice has been increased by 1.5 times in this decade (2011–2020) as compared to the previous decade (2000–2010) (Dey et al., 2020). The Ganga river is one of the primary sources of irrigation in this region, along with the groundwater. The usage of river water for irrigation also slows the flow rate of the river in this region. The river experts have reported in the media that the greenish color of the river in this region during May–June 2021 could have occurred due to the low flow condition of the river. Some construction work had been taking place near the river Ganga in this region, which diminishes the flow rate in the region as per media reports.

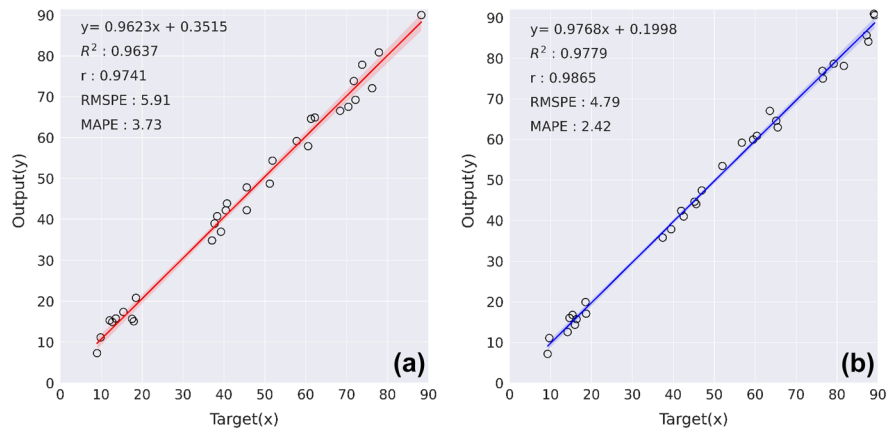

Fig. 10 Regression plot and associated statistical parameters for the test data points for **a** MLP **b** RBF at 17 and 15 nodes, respectively (MAPE and RMSPE values are in %)

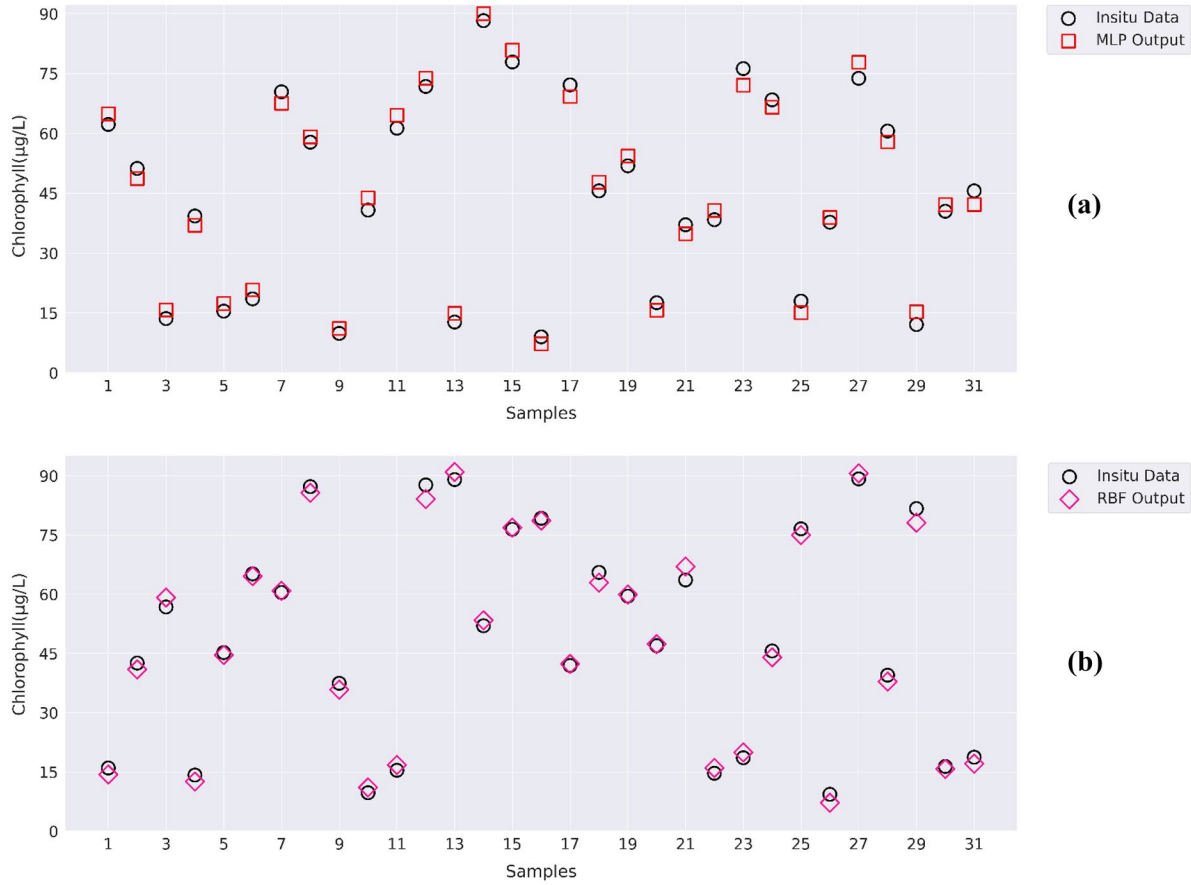

Fig. 11 Scatter plot showing a comparison between observed in situ values and predicted Chl-a concentration using neural network architectures: **a** MLP, **b** RBF

Another consequence of the low flow or stable water condition has been the thermal stratification. The high water temperature has also been considered an additional factor for thermal stratification. Thermal stratification occurs when the lower layer remains cooler and the top layer of the water column becomes warmer (Zhu et al., 2013). When a water body has been stratified, lower layer waters often become exhausted with oxygen (anoxia), leading to increased nutrient release from the sediments. The pulses of nutrients from the colder bottom layer may enhance the algal growth in the uppermost layer of the water body (Weinke & Biddanda, 2019). Due to climate change, the temperature of the river Ganga has increased (Tripathi et al., 2017), which leads to thermal stratification. The stratification will eventually give rise to the algal growth in the river.

Another factor for enhanced algal growth in this region may be the low turbidity of the river in this region. A significant part of the year 2020 has been under the effect of lockdown due to the novel Coronavirus. The Indian government has applied the lockdown in the entire country for most of the year 2020 (Chauhan & Singh, 2020; Patel et al., 2020). Due to

(a) 15 May 2021

(b) 30 May 2021

(c) 14 June 2021

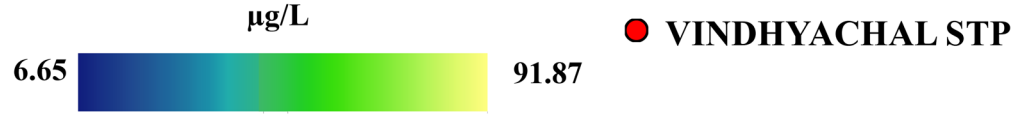

◂**Fig. 12** Spatial variation in Chl-a concentration in the study stretch using RBF predicted values on **a** 15 May, **b** 30 May, and **c** 14 June 2021

the effect of the lockdown, all the rivers in the country, including the river Ganga, have become cleaner, so the turbidity in the river gets reduced (Garg et al., 2020). The algal growth surge in the low turbid condition. More solar radiation can infiltrate through the water column when the water has become less turbid, and solar radiation plays a critical role in algal growth. This creates optimal conditions for algal growth (Singh & Singh, 2015; Wellard Kelly et al., 2013). The discharge from the Vindhyachal sewage treatment plant(STP) has been considered the primary cause of the algal bloom in the region, as per the reports submitted to the Varanasi district magistrate (DM) (Vindhyachal STP discharge causing algal bloom in Ganga, 2021).

From the above discussion, it can be seen that this menace of algal bloom in the river Ganga in the Mirzapur-Varanasi region is an outcome of several factors that have been accompanying each other.

Conclusion

This study has been performed to detect the concentration of the Chl-a in the Varanasi and nearby regions using S-2 satellite imageries. The period of analysis has been considered between May and June 2021. The spatial distribution of the Chl-a concentration has been simulated using satellite imageries and ANN. Two of the ANN models have been used in this study, namely MLP and RBF. The RBF model shows better-simulating results in comparison to that of the MLP model. The RBF has the lower error values (RMSPE = 4.79%, MAPE = 2.42%) as compared to MLP (RMSPE = 5.91%, MAPE = 3.73%). The Chl-a concentration can represent the spread of algal bloom in the river. The probable causes of this algal bloom generation have also been analyzed. According to this study, the algal bloom concentration became highest on 14 June 2021. These blooms turn the river water green. These blooms are very harmful to the river ecosystem as they can disrupt the fish network structure of the river; alongside, these blooms can also cause the death of several other organisms that reside

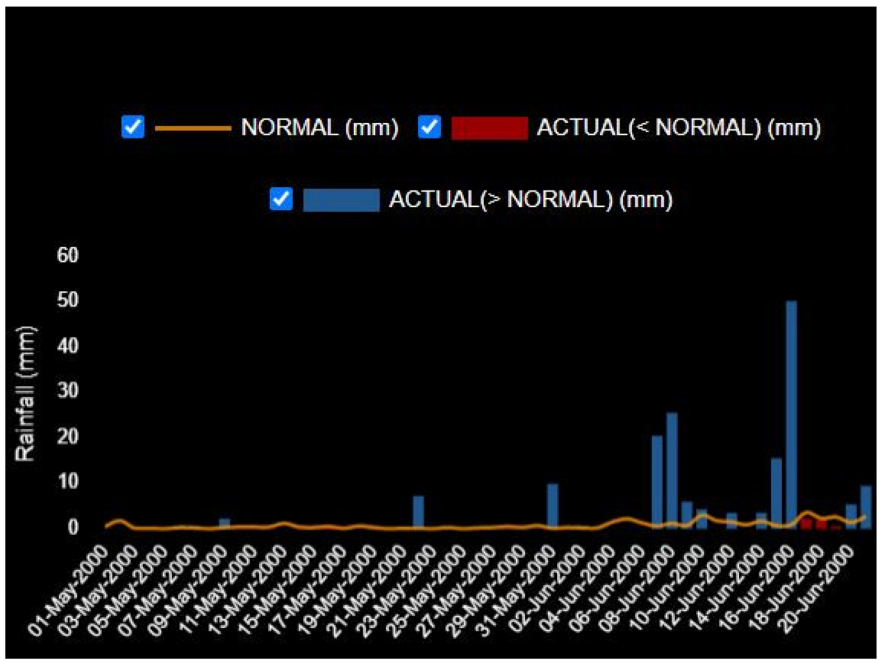

Fig. 13 Rainfall graph for the Varanasi and nearby region for the time period May–June 20, 2000. The spectral signature curve has been prepared in Erdas IMAGINE 2014 software. The violin plot, scatter plots have been made by using GOOGLE-COLAB (open-source software). The logical Venn diagram has been made in MS PowerPoint

inside the river. When the river becomes flooded in the monsoon period, the flow of the river increases tremendously, which can destroy these blooms as well. For the sake of the river ecosystem restoration, it is important to eradicate these harmful blooms as early as possible.

Acknowledgements The authors would like to take this opportunity to express their gratefulness to Dr. Prabhat Kumar Singh Dixit, HOD of Civil Engineering Department, IIT (BHU), for constantly motivating us to carry forward this study. Additionally, a special vote of thanks to Dr. Prithvish Nag (former Surveyor General of India) for reviewing and adding positive comments to this manuscript.

Funding Not applicable.

Data availability Data had been accessed through the GEE platform. https://earthengine.google.com. (accessed on 20 June 2021). The rainfall dataset had been downloaded from the INDIA WRIS portal. https://indiawris.gov.in/wris/ (accessed on 2 July 2021).

Declarations

Conflict of interest The authors declare no competing interests.

References

Bansal, R. (2017). Radial basis function network. Hackerearth. Retrieved August 14, 2021, from https://www.hackerearth.com/blog/developers/radial-basis-function-network/

Bhattacharjee, R., Choubey, A., Das, N., Ohri, A., & Gaur, S. (2021). Detecting the carotenoid pigmentation due to haloarchaea microbes in the Lonar Lake, Maharashtra, India Using Sentinel-2 Images. *Journal of the Indian Society of Remote Sensing, 49*(2), 305–316. https://doi.org/10.1007/s12524-020-01219-z

Boucher, J., Weathers, K. C., Norouzi, H., & Steele, B. (2018). Assessing the effectiveness of Landsat 8 chlorophyll a retrieval algorithms for regional freshwater monitoring. *Ecological Applications, 28*(4), 1044–1054. https://doi.org/10.1002/eap.1708

Bowes, M. J., Read, D. S., Joshi, H., Sinha, R., Ansari, A., Hazra, M., Simon, M., Vishwakarma, R., Armstrong, L. K., Nicholls, D. J., & Rees, H. G. (2020). Nutrient and microbial water quality of the upper Ganga River, India: Identification of pollution sources. *Environmental Monitoring and Assessment, 192*(8), 1–20. https://doi.org/10.1007/s10661-020-08456-2

Bramich, J., Bolch, C. J., & Fischer, A. (2021). Improved red-edge chlorophyll-a detection for Sentinel 2. *Ecological Indicators, 120*, 106876. https://doi.org/10.1016/j.ecolind.2020.106876

Bresciani, M., Cazzaniga, I., Austoni, M., Sforzi, T., Buzzi, F., Morabito, G., & Giardino, C. (2018). Mapping phytoplankton blooms in deep subalpine lakes from Sentinel-2A and Landsat-8. *Hydrobiologia, 824*(1), 197–214. https://doi.org/10.1007/s10750-017-3462-2

Bronowicka-Mielniczuk, U., Mielniczuk, J., Obroślak, R., & Przystupa, W. (2019). A comparison of some interpolation techniques for determining spatial distribution of nitrogen compounds in groundwater. *International Journal of Environmental Research, 13*(4), 679–687. https://doi.org/10.1007/s41742-019-00208-6

Budd, J. W., Beeton, A. M., Stumpf, R. P., Culver, D. A., & Charles Kerfoot, W. (2001). Satellite observations of Microcystis blooms in western Lake Erie. *Internationale Vereinigung Für Theoretische Und Angewandte Limnologie: Verhandlungen, 27*(7), 3787–3793. https://doi.org/10.1080/03680770.1998.11901692

Chauhan, A., & Singh, R. P. (2020). Decline in PM2. 5 concentrations over major cities around the world associated with COVID-19. *Environmental Research*, *187*, 109634. https://doi.org/10.1016/j.envres.2020.109634

Chen, J., Zhu, W., Tian, Y. Q., Yu, Q., Zheng, Y., & Huang, L. (2017). Remote estimation of colored dissolved organic matter and chlorophyll-a in Lake Huron using Sentinel-2 measurements. *Journal of Applied Remote Sensing, 11*(3), 036007. https://doi.org/10.1117/1.JRS.11.036007

Das, N., Ohri, A., Agnihotri, A. K., Omar, P. J., & Mishra, S. (2020). wetland dynamics using geo-spatial technology. In A. AlKhaddar, R. Singh, S. Dutta, & M. Kumari (Eds.), *Advances in Water Resources Engineering and Management*, (37th ed., pp 237–244). Springer.

Davydov, O., & Oanh, D. T. (2011). On the optimal shape parameter for Gaussian radial basis function finite difference approximation of the Poisson equation. *Computers & Mathematics with Applications, 62*(5), 2143–2161. https://doi.org/10.1016/j.camwa.2011.06.037

Devi, R., Tesfahune, E., Legesse, W., Deboch, B., & Beyene, A. (2008). Assessment of siltation and nutrient enrichment of Gilgel Gibe dam. *Southwest Ethiopia. Bioresource Technology, 99*(5), 975–979. https://doi.org/10.1016/j.biortech.2007.03.013

Dey, S., Bhatt, D., Haq, S., & Mall, R. K. (2020). Potential impact of rainfall variability on groundwater resources: A case study in Uttar Pradesh. *India. Arabian Journal of Geosciences, 13*(3), 1–11. https://doi.org/10.1007/s12517-020-5083-8

Dixit, R. B., Patel, A. K., Toppo, K., & Nayaka, S. (2017). Emergence of toxic cyanobacterial species in the Ganga River, India, due to excessive nutrient loading. *Ecological Indicators, 72*, 420–427. https://doi.org/10.1016/j.ecolind.2016.08.038

Duan, H., Zhang, Y., Zhang, B., Song, K., & Wang, Z. (2007). Assessment of chlorophyll-a concentration and trophic state for Lake Chagan using Landsat TM and field spectral data. *Environmental Monitoring and Assessment*, *129*(1), 295–308. https://doi.org/10.1007/s10661-006-9362-y

Garg, V., Aggarwal, S. P., & Chauhan, P. (2020). Changes in turbidity along Ganga River using Sentinel-2 satellite data during lockdown associated with COVID-19. *Geomatics, Natural Hazards and Risk*, *11*(1), 1175–1195. https://doi.org/10.1080/19475705.2020.1782482

Gholizadeh, M. H., Melesse, A. M., & Reddi, L. (2016). A comprehensive review on water quality parameters

estimation using remote sensing techniques. *Sensors, 16*(8), 1298. https://doi.org/10.3390/s16081298

Gorelick, N., Hancher, M., Dixon, M., Ilyushchenko, S., Thau, D., & Moore, R. (2017). Google Earth Engine: Planetary-scale geospatial analysis for everyone. *Remote Sensing of Environment, 202*, 18–27. https://doi.org/10.1016/j.rse.2017.06.031

Gorji, T., Yildirim, A., Hamzehpour, N., Tanik, A., & Sertel, E. (2020). Soil salinity analysis of Urmia Lake Basin using Landsat-8 OLI and Sentinel-2A based spectral indices and electrical conductivity measurements. *Ecological Indicators, 112*, 106173. https://doi.org/10.1016/j.ecolind.2020.106173

Guo, Q., Wu, X., Bing, Q., Pan, Y., Wang, Z., Fu, Y., Wang, D., & Liu, J. (2016). Study on retrieval of chlorophyll-a concentration based on Landsat OLI Imagery in the Haihe River. *China. Sustainability, 8*(8), 758. https://doi.org/10.3390/su8080758

Ha, N. T. T., Koike, K., Nhuan, M. T., Canh, B. D., Thao, N. T. P., & Parsons, M. (2017a). Landsat 8/OLI two bands ratio algorithm for chlorophyll-a concentration mapping in hypertrophic waters: An application to West Lake in Hanoi (Vietnam). *IEEE Journal of Selected Topics in Applied Earth Observations and Remote Sensing, 10*(11), 4919–4929. https://doi.org/10.1109/JSTARS.2017.2739184

Ha, N. T. T., Thao, N. T. P., Koike, K., & Nhuan, M. T. (2017b). Selecting the best band ratio to estimate chlorophyll-a concentration in a tropical freshwater lake using sentinel 2A images from a case study of Lake Ba Be (Northern Vietnam). *ISPRS International Journal of Geo-Information, 6*(9), 290. https://doi.org/10.3390/ijgi6090290

Han, L., & Jordan, K. J. (2005). Estimating and mapping chlorophyll-a concentration in Pensacola Bay, Florida using Landsat ETM+ data. *International Journal of Remote Sensing, 26*(23), 5245–5254. https://doi.org/10.1080/01431160500219182

Haritash, A. K., Gaur, S., & Garg, S. (2016). Assessment of water quality and suitability analysis of River Ganga in Rishikesh. *India. Applied Water Science, 6*(4), 383–392. https://doi.org/10.1007/s13201-014-0235-1

Huete, A. R. (2004). Remote sensing for environmental monitoring. In *Environmental monitoring and characterization* (pp. 183–206). Academic Press. https://doi.org/10.1016/B978-012064477-3/50013-8

Jaiswal, D., & Pandey, J. (2019). Investigations on peculiarities of land-water interface and its use as a stable testbed for accurately predicting changes in ecosystem responses to human perturbations: A sub-watershed scale study with the Ganga River. *Journal of Environmental Management, 238*, 178–193. https://doi.org/10.1016/j.jenvman.2019.02.126

Jaiswal, R. (2021). Ganga turns green in Varanasi during Covid-19 second wave; Scientists explain why and how. Resource Document. INDIA TODAY. Retrieved July 2, 2021, from https://www.indiatoday.in/india/story/ganga-turns-green-in-varanasi-during-covid-19-second-wave-scientists-explain-why-and-how-1807631-2021-05-27

Kopal, I., Harničárová, M., Valíček, J., Krmela, J., & Lukáč, O. (2019). Radial basis function neural network-based modeling of the dynamic thermo-mechanical response and damping behavior of thermoplastic elastomer systems. *Polymers, 11*(6), 1074. https://doi.org/10.3390/polym11061074

Lee, J. H. W., Hodgkiss, I. J., Wong, K. T. M., & Lam, I. H. Y. (2005). Real time observations of coastal algal blooms by an early warning system. *Estuarine, Coastal and Shelf Science, 65*(1–2), 172–190. https://doi.org/10.1016/j.ecss.2005.06.005

Li, L., Yang, J., & Wu, J. (2019). A method of watershed delineation for flat terrain using sentinel-2a imagery and DEM: A case study of the Taihu basin. *ISPRS International Journal of Geo-Information, 8*(12), 528. https://doi.org/10.3390/ijgi8120528

Markogianni, V., Dimitriou, E., & Tzortziou, M. (2013, August). Monitoring of chlorophyll-a and turbidity in Evros River (Greece) using Landsat imagery. In *First International Conference on Remote Sensing and Geoinformation of the Environment (RSCy2013)* (Vol. 8795, p. 87950R). International Society for Optics and Photonics. https://doi.org/10.1117/12.2027047

Mas, J. F., & Flores, J. J. (2008). The application of artificial neural networks to the analysis of remotely sensed data. *International Journal of Remote Sensing, 29*(3), 617–663. https://doi.org/10.1080/01431160701352154

Mishra, V. N., Rai, P. K., Prasad, R., Punia, M., & Nistor, M. M. (2018). Prediction of spatio-temporal land use/land cover dynamics in rapidly developing Varanasi district of Uttar Pradesh, India, using geospatial approach: A comparison of hybrid models. *Applied Geomatics, 10*(3), 257–276. https://doi.org/10.1007/s12518-018-0223-5

Misra, M. (2019). Rivers are critical for groundwater recharge. Resource Document. HINDUSTAN TIMES. Retrieved June 20, 2021, from https://www.hindustantimes.com/analysis/rivers-are-critical-for-groundwater-recharge/story-HWP3WocyCwRhz8ho98jOcL.html

Nguyen, L. T. K., & Keip, M. A. (2018). A data-driven approach to nonlinear elasticity. *Computers & Structures, 194*, 97–115. https://doi.org/10.1016/j.compstruc.2017.07.031

Pai, D. S., Rao, A. S., Senroy, S., Pradhan, M., Pillai, P. A., & Rajeevan, M. (2017). Performance of the operational and experimental long-range forecasts for the 2015 southwest monsoon rainfall. *Current Science*, 68–75. https://www.jstor.org/stable/24911618

Palani, S., Liong, S. Y., & Tkalich, P. (2008). An ANN application for water quality forecasting. *Marine Pollution Bulletin, 56*(9), 1586–1597. https://doi.org/10.1016/j.marpolbul.2008.05.021

Palmer, S. C., Kutser, T., & Hunter, P. D. (2015). Remote sensing of inland waters: Challenges, progress and future directions. *Remote Sensing of Environment, 157*, 1–8. https://doi.org/10.1016/j.rse.2014.09.021

Pandey, J., & Singh, R. (2017). Heavy metals in sediments of Ganga River: Up-and downstream urban influences. *Applied Water Science, 7*(4), 1669–1678. https://doi.org/10.1007/s13201-015-0334-7

Patel, P. P., Mondal, S., & Ghosh, K. G. (2020). Some respite for India's dirtiest river? Examining the Yamuna's water quality at Delhi during the COVID-19 lockdown period. *Science of the Total Environment, 744*, 140851. https://doi.org/10.1016/j.scitotenv.2020.140851

Pislaru, C., & Shebani, A. (2014). Identification of nonlinear systems using radial basis function neural network. *International*

Journal of Computer, Information, Systems and Control Engineering, 8(9), 1528–1533.

Prasad, S., Saluja, R., & Garg, J. K. (2020). Assessing the efficacy of Landsat-8 OLI imagery derived models for remotely estimating chlorophyll-a concentration in the Upper Ganga River. *India. International Journal of Remote Sensing, 41*(7), 2439–2456. https://doi.org/10.1080/01431161.2019.1688888

Rai, P. K., Mishra, A., & Tripathi, B. D. (2010). Heavy metal and microbial pollution of the River Ganga: A case study of water quality at Varanasi. *Aquatic Ecosystem Health & Management, 13*(4), 352–361. https://doi.org/10.1080/14634988.2010.528739

Ressom, H., Miller, R. L., Natarajan, P., & Slade, W. H. (2007). Computational intelligence and its application in remote sensing. In R. L. Miller, C. E. Del Castillo, & B. A. Mckee (Eds.), *Remote Sensing of Coastal Aquatic Environments*, (7th ed., pp. 205–227). Springer.

Roy, P. S., Behera, M. D., & Srivastav, S. K. (2017). Satellite remote sensing: Sensors, applications and techniques. *Proceedings of the National Academy of Sciences, India Section a: Physical Sciences, 87*(4), 465–472. https://doi.org/10.1007/s40010-017-0428-8

Rundquist, D. C., Han, L., Schalles, J. F., & Peake, J. S. (1996). Remote measurement of algal chlorophyll in surface waters: The case for the first derivative of reflectance near 690 nm. *Photogrammetric Engineering and Remote Sensing, 62*(2), 195–200.

Saxena, S., & Singh, P. K. (2020). Assessment of health of river Ganga at Varanasi, India. https://doi.org/10.46488/NEPT.2020.v19i03.004

Singh, B. (2021). Uttar Pradesh: Origin of algal bloom to be traced. Resource Document. TIMES OF INDIA. Retrieved June 22, 2021, from http://timesofindia.indiatimes.com/articleshow/83352950.cms?utm_source=contentofinterest&utm_medium=text&utm_campaign=cppst

Singh, K. P., Basant, A., Malik, A., & Jain, G. (2009). Artificial neural network modeling of the river water quality—A case study. *Ecological modelling*, *220*(6), 888–895. https://doi.org/10.1016/j.ecolmodel.2009.01.004.

Singh, S. P., & Singh, P. (2015). Effect of temperature and light on the growth of algae species: A review. *Renewable and Sustainable Energy Reviews, 50*, 431–444. https://doi.org/10.1016/j.rser.2015.05.024

Tare, V., Yadav, A. V. S., & Bose, P. (2003). Analysis of photosynthetic activity in the most polluted stretch of river Ganga. *Water Research, 37*(1), 67–77. https://doi.org/10.1016/S0043-1354(01)00385-2

Tripathi, A., Kumar, N., & Chauhan, D. K. (2017). Understanding integrated impacts of climate change and pollution on Ganges river system: A mini review on biological effects, knowledge gaps and research needs. *SM J Biol, 3*(1), 1017.

Trivedi, R. C. (2010). Water quality of the Ganga River–An overview. *Aquatic Ecosystem Health & Management, 13*(4), 347–351. https://doi.org/10.1080/14634988.2010.528740

Van der Werff, H., & Van der Meer, F. (2016). Sentinel-2A MSI and Landsat 8 OLI provide data continuity for geological remote sensing. *Remote Sensing, 8*(11), 883. https://doi.org/10.3390/rs8110883

Van Vliet, M. T. H., Ludwig, F., Zwolsman, J. J. G., Weedon, G. P., & Kabat, P. (2011). Global river temperatures and sensitivity to atmospheric warming and changes in river flow. *Water Resources Research*, *47*(2). https://doi.org/10.1029/2010WR009198

Vindhyachal STP discharge causing algal bloom in Ganga. (n.d.). Resource Document. TIMES OF INDIA. Retrieved June 22, 2021, from https://timesofindia.indiatimes.com/city/varanasi/vindhyachal-stp-discharge-causing-algal-bloom-in-ganga/articleshow/83468686.cms

Wang, C., Wang, Z., Wang, P., & Zhang, S. (2016). Multiple effects of environmental factors on algal growth and nutrient thresholds for harmful algal blooms: Application of response surface methodology. *Environmental Modeling & Assessment, 21*(2), 247–259. https://doi.org/10.1007/s10666-015-9481-3

Weinke, A. D., & Biddanda, B. A. (2019). Influence of episodic wind events on thermal stratification and bottom water hypoxia in a Great Lakes estuary. *Journal of Great Lakes Research, 45*(6), 1103–1112. https://doi.org/10.1016/j.jglr.2019.09.025

Wellard Kelly, H. A., Rosi-Marshall, E. J., Kennedy, T. A., Hall, R. O., Jr., Cross, W. F., & Baxter, C. V. (2013). Macroinvertebrate diets reflect tributary inputs and turbidity-driven changes in food availability in the Colorado River downstream of Glen Canyon Dam. *Freshwater Science, 32*(2), 397–410. https://doi.org/10.1899/12-088.1

Xu, X., & Gupta, N. (2019). Artificial neural network approach to predict the elastic modulus from dynamic mechanical analysis results. *Advanced Theory and Simulations, 2*(4), 1800131. https://doi.org/10.1002/adts.201800131

Zanchett, G., & Oliveira-Filho, E. C. (2013). Cyanobacteria and cyanotoxins: From impacts on aquatic ecosystems and human health to anticarcinogenic effects. *Toxins, 5*(10), 1896–1917. https://doi.org/10.3390/toxins5101896

Zhu, K., Bi, Y., & Hu, Z. (2013). Responses of phytoplankton functional groups to the hydrologic regime in the Daning River, A tributary of Three Gorges Reservoir, China. *Science of the Total Environment, 450*, 169–177. https://doi.org/10.1016/j.scitotenv.2013.01.101

Zurqani, H. A., Post, C. J., Mikhailova, E. A., Schlautman, M. A., & Sharp, J. L. (2018). Geospatial analysis of land use change in the Savannah River Basin using Google Earth Engine. *International Journal of Applied Earth Observation and Geoinformation, 69*, 175–185. https://doi.org/10.1016/j.jag.2017.12.006